Materials Today Bio 30 (2025) 101378

Contents lists available at ScienceDirect

Materials Today Bio

journal homepage: www.journals.elsevier.com/materials-today-bio

Hyaluronidase-responsive hydrogel loaded with magnetic nanoparticles combined with external magnetic stimulation for spinal cord injury repair

Zhiyi Fan [a,b,1], Guofu Zhang [a,b,1], Wanda Zhan [a,b], Juehan Wang [d], Chaoyong Wang [e], QianYing Yue [f], Zhangheng Huang [c,**], Yongxiang Wang [a,b,*]

[a] Northern Jiangsu People's Hospital, Yangzhou, Jiangsu, China
[b] Northern Jiangsu People's Hospital Affiliated to Yangzhou University, Yangzhou, Jiangsu, China
[c] First Affiliated Hospital of Wenzhou Medical University, Wenzhou, Zhejiang, China
[d] Department of Orthopaedics and Traumatology, School of Clinical Medicine, Li Ka Shing Faculty of Medicine, The University of Hong Kong, Pokfulam, Hong Kong
[e] Northern Jiangsu People's Hospital, Clinical Teaching Hospital of Medical School, Nanjing University, Yangzhou, China
[f] Jockey Club School of Public Health and Primary Care, The Chinese University of Hong Kong, Hong Kong

ARTICLE INFO

Keywords:
Spinal cord injury
Hyaluronidase
Magnetic field
Hydrogel

ABSTRACT

Spinal cord injury (SCI) is a neurological condition that causes significant loss of sensory, motor, and autonomic functions below the level of injury. Current clinical treatment strategies often fail to meet expectations. Hyaluronidase is typically associated with tumor progression and bacterial infections. Analysis showed that hyaluronidase also persistently increased in a rat total excision model. In this study, we designed a highly biocompatible dual-responsive hydrogel. Hyaluronic acid (HA)-Gelatin (Gel) served as the base for the hydrogel, crosslinked via an amide reaction to form the hydrogel. The hydrogel was further combined with Neurotrophic growth factor (NGF) and Fe_3O_4 nanoparticles, exhibiting low toxicity, good mechanical properties, self-healing ability, and sustained drug release. In cellular experiments, the novel hydrogel significantly promoted neural axon growth and development under an external magnetic field. Therapeutic results were confirmed in a rat spinal cord resection model, where inflammation was reduced, chondroitin sulfate proteoglycans decreased and a favorable environment for nerve regeneration was provided; neural regeneration improved hind limb motor function in SCI rats. These results underscore the therapeutic potential of hydrogel.

1. Introduction

The spinal cord stands as one of the pivotal constituents of the central nervous system, serving as the principal conduit linking the brain with the peripheral nerves. Unfortunately, spinal cord injury (SCI) can lead to a partial or complete cessation of function beneath the point of injury, stemming from an array of underlying causes [1]. This injury is characterized by a marked impairment or complete loss of sensory and motor function beneath the affected level, giving rise to sensory and motor deficiencies, and in severe instances, even paralysis. Additionally, SCI can precipitate a myriad of complications, including decubitus ulcers, urinary tract infections, cardiovascular irregularities, and sensory disturbances, which in extreme cases, can culminate in respiratory failure. At present, the cornerstone of SCI management revolves around surgical interventions. Nevertheless, in instances where the injury is severe, it may still progress to respiratory failure [2–4]. The current repertoire of treatments for SCI primarily encompasses surgical decompression and methylprednisolone shock therapy. However, these modalities often fall short of the desired therapeutic outcomes and are accompanied by a plethora of adverse effects, thereby underscoring the pressing need for

Abbreviations: SCI, Spinal cord injury; Gel, Gelatin; NGF, Neurotrophic growth factor; HA, Hyaluronic acid; GAG, Glycosaminoglycan; mT, Millitesla; FBS, Fetal bovine serum; DAPI, 4′,6-diamidino-2-phenylindole; DMEM, Dulbecco's modified Eagle's medium; SD, Sprague Dawley; SEM, Scanning electron microscopy; TUJ1, Class III βtubulin; GAP43, Growth-associated protein 43; MEP, Motor evoked potential; H&E, Hematoxylin and Eosin; LFB, Luxol fast blue; CSPGs, Chondroitin sulfate proteoglycans..

* Corresponding author. Northern Jiangsu People's Hospital, Yangzhou, Jiangsu, China.
** Corresponding author. First Affiliated Hospital of Wenzhou Medical University, Nanbaixiang Street, Ouhai District, Wenzhou, Zhejiang, China.
E-mail addresses: hzh1319330149@sina.com (Z. Huang), wyx918spine@yzu.edu.cn (Y. Wang).
[1] These authors contributed equally to this work.

https://doi.org/10.1016/j.mtbio.2024.101378
Received 15 September 2024; Received in revised form 8 November 2024; Accepted 3 December 2024
Available online 6 December 2024

the development of more efficacious clinical treatments [5,6].

Tissue engineering stands as a multifaceted technological marvel, intricately weaving together cells, drugs, molecules, and advanced biomaterials. This interdisciplinary endeavor offers an innovative and promising avenue for the repair of SCI, ushering in a new era of therapeutic possibilities. At its core, tissue engineering harnesses the potential of various materials as efficient delivery vehicles, transporting cells or drugs precisely to the desired site of action or facilitating their localized placement in situ. This ingenious approach mitigates the limitations posed by the solitary application of cells or drugs, namely their slow proliferation or inadequate local concentration. By amplifying their therapeutic efficacy, tissue engineering not only fills the void left by damaged tissue but also meticulously modulates the local microenvironment, fostering a conducive environment for repair and regeneration [7].

Stimuli-responsive materials, often referred to as smart or environmentally sensitive materials, possess the remarkable capability to undergo transformations such as protonation, hydrolysis, alterations in hydrophilicity, or adjustments in molecular conformation, all in response to specific environmental stimuli [8]. They exhibit a remarkable capacity to make feedback adjustments in harmony with external signals. The recent advancements in the realms of human physiology and pathology research, along with significant strides in materials chemistry, biomolecules, pharmaceutical sciences, and nanotechnology, have collectively facilitated the integration of these responsive materials into the biomedicine sector. These "smart" biomaterials, which demonstrate exquisite sensitivity to specific biosignals or pathological abnormalities, play a pivotal role in realizing the vision of precision medicine. Their applications span a wide array of medical endeavors, including but not limited to drug delivery and release systems, disease diagnosis and treatment methodologies, tissue engineering initiatives, and the development of innovative biomedical devices.

Hyaluronic acid (HA), a unique form of linear glycosaminoglycan (GAG), is constructed from a repetitive pattern of disaccharide units, specifically consisting of D-glucuronic acid and N-acetylglucosamine. Renowned for its hydrophilic and viscoelastic properties, HA holds pivotal roles in a vast array of biological processes [9,10]. The discovery of hyaluronidase dates back to 1939, when Chain and Duthie isolated the enzymes from animal testis extracts and bacterial filtrates. Functioning as a "diffusion catalyst," these enzymes expedite the dispersion of injected dyes and toxins, facilitating their distribution throughout the body [11]. Subsequent research endeavors have unveiled the specificity of several hyaluronidase enzymes, which demonstrate a pronounced capacity to degrade HA while exhibiting minimal activity towards other GAGs, such as dermatan sulfate and chondroitin sulfate [12]. This selectivity underscores the enzymes' potential for targeted therapeutic interventions. Intriguingly, following SCI, hyaluronidase enzymes are naturally produced at the site of damage, persisting for an extended duration of at least six weeks [13]. Therefore, we hope to use these enzymes to create enzyme-responsive materials loaded with neurotrophic factors to improve SCI prognosis.

Magnetic stimulation in the millitesla (mT) range (Such as: 300 MT) does not cause phototoxicity or thermotoxicity, making it a safer option. Low-frequency weak magnetic fields are commonly used in clinical practice to promote stem cell proliferation and differentiation, reduce inflammation and edema, relieve pain, decrease apoptosis, and enhance tissue regeneration. They also promote the expression of growth factors like FGF and VEGF, aiding in reducing inflammation and promoting blood vessel regeneration [14–17]. Fe_3O_4 nanoparticles are commonly used magnetic nanomaterials. When Fe_3O_4 nanoparticles are smaller than 20 nm, they exhibit superparamagnetic properties. Without an applied magnetic field, the particles exhibit only irregular thermal motions and no external magnetic properties. However, when a magnetic field is applied, the particles align with the field, and the Fe_3O_4 nanoparticles respond accordingly [18].

In this study, we analyzed the presence of hyaluronidase following SCI. Based on the results, we designed an enzyme/magnetic dual-responsive hydrogel delivery platform with high biocompatibility and good mechanical properties. The purpose of this platform is to transport and continuously release NGF to the site of injury through the properties of hyaluronic acid that respond to hyaluronidase, and through external magnetic field stimulation, to improve the local environment of the injury site, promoting neurogenesis, as shown in Fig. 1.

2. Materials and methods

2.1. Materials and animals

Hyaluronic acid (HA, Mw: 10–50 kDa) and Gelatin (Gel) was obtained from Focus Biotech (Shanghai, China). Fe_3O_4 nanoparticles were purchased from Feynman Nano (Zhengzhou, China). Neurotrophic growth factor (NGF) from Sigma-Aldrich Corporation (USA). Penicillin-streptomycin, trypsin-EDTA, and fetal bovine serum (FBS) were obtained from Gibco (Carlsbad, CA). CCK-8 kit, live/dead kit, Hurst, and 4′,6-diamidino-2-phenylindole (DAPI) were purchased from Beyotime (Shanghai, China). Phenochromocytoma cells 12 (PC-12) were sourced from the National Certified Cell Culture Collection Center (Shanghai, China). Dulbecco's modified Eagle's medium (DMEM) were obtained from Saibecon (Shanghai, China). 300 MT NdFeB magnet square from Tiansheng company (Shenzhen, China).

Female Sprague Dawley (SD) rats, 9 weeks old, n = 50, with a mean weight of 40 g. Rats were housed in a 12-h light/dark cycle per laboratory regulations and maintained at 20–22 °C with 50 % relative humidity. This study was approved by the Animal Experimental Ethics Committee of the Yangzhou University (yzu-lcyxy-n472). Animal feeding and welfare tests were performed according to the standards of the Laboratory of Yangzhou.

2.2. Synthesis and characterization of HA-Gel@NGF + Fe_3O_4 hydrogel

The HA-Gel hydrogel was prepared using a chemical crosslinking double syringe method. The preparation process was as follows: First, a dilute HCl solution with pH 4.7 was prepared. A certain amount of Gel was added to a beaker, followed by deionized water to form a 15 % aqueous Gel solution. This mixture was placed on a magnetic stirrer at 45 °C and 1000 rpm and stirred until a clear Gel solution was obtained. Next, 0.3 g of HA was placed in a beaker with 30 ml of dilute HCl solution at 25 °C and stirred at 800 rpm on a magnetic stirrer to form a clear HA solution. Then, 0.3 g of EDC was added to the solution and stirring continued for 1 h. The solution was adjusted to pH 4.7 using 0.1 M HCl. In order to determine the content of Fe_3O_4 nanoparticles without affecting the gelation of the hydrogel, 0.5 ml of Gel solution and 0.5 ml of HA solution were mixed with 10.0 μg of NGF and Fe_3O_4 nanoparticles (with Fe_3O_4 contents of 0, 3, 5, 7 mg respectively). After mixing, the hydrogel was obtained through appropriate stirring. After mixing, the HA-Gel@NGF + Fe_3O_4 hydrogel was obtained by appropriate stirring. After mixing, HA-Gel@NGF + Fe_3O_4 hydrogel with different concentrations of Fe_3O_4 nanoparticles were obtained through appropriate stirring.

The hysteresis loop reflects the relationship between the magnetization intensity and the magnetic field strength of ferromagnetic materials during the magnetization process, serving as an important indicator for the study of magnetic materials. First, 25 mg of HA-Gel@NGF+0 mg Fe_3O_4, HA-Gel@NGF+3 mg Fe_3O_4, HA-Gel@NGF+5 mg Fe_3O_4, and HA-Gel@NGF+7 mg Fe_3O_4 hydrogel are weighed separately and placed into a circular sample tube, with the test temperature set at 294.5 K. Using the TD8320 permanent magnet material testing system, magnetic response analysis of the hydrogel is conducted within the range of −4000 to 4000 Oe. By comparing the changes in the saturation magnetization and coercivity of hydrogel prepared with four different feed ratios, the magnetic response characteristics of the hydrogel to external magnetic fields are explained.

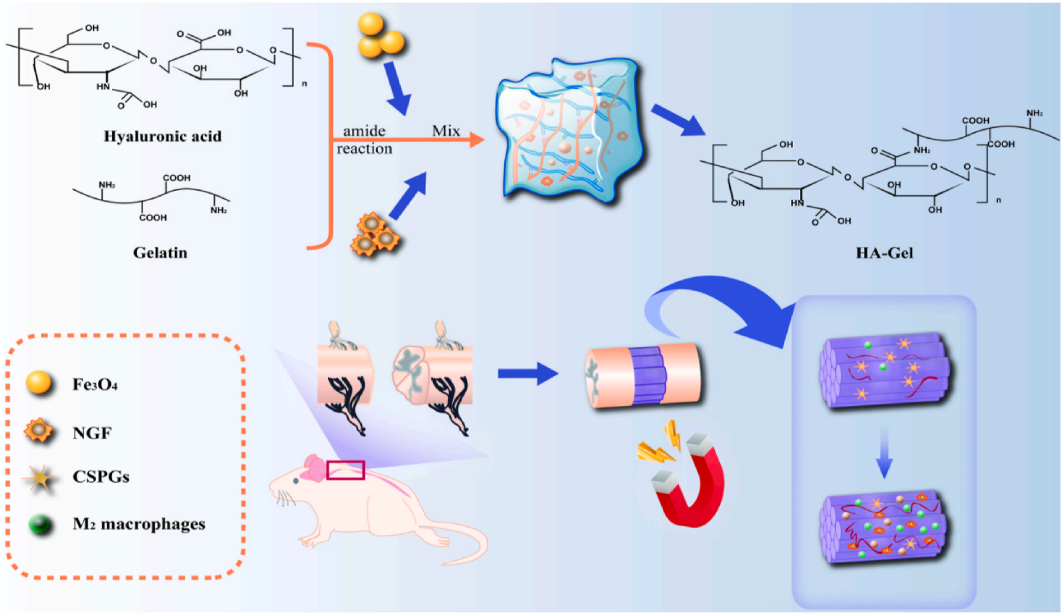

Fig. 1. Preparation strategy of HA-Gel@NGF + Fe_3O_4 hydrogel and its application in SCI. Schematic diagram of HA-Gel@NGF + Fe_3O_4 hydrogel synthesis. The HA-Gel@NGF + Fe_3O_4 hydrogel possesses remarkable multifunctionality and excellent chemical, biological, and mechanical properties. By encapsulating NGF and Fe_3O_4 within its porous structure, it exhibits the desired release characteristics. After SCI, there is an increase in hyaluronidase and chondroitin sulfate protein, with axonal disruption. Following implantation of HA-Gel@NGF + Fe_3O_4 hydrogel, external magnetic stimulation can improve the spinal cord microenvironment and promote neural axon regeneration.

We selected the 170SX Fourier Transform Infrared Spectrometer to characterize the HA-Gel hydrogel, detecting its functional groups, ester and amide groups, to see if the Gel and HA substances are combined together. We first took samples of Gel, HA, and HA-Gel, and ground them into a powder, mixing with potassium bromide to prepare the samples for pressing. The infrared spectrum scanning range is 4000–400 cm-1, with a resolution of 4 cm-1. Through FTIR analysis, we examined the characteristic peaks of each component in the composite hydrogel and analyzed the possible interactions between the components.

2.3. Gelation time, scanning electron microscopy (SEM) and compression testing

Gelation time was ascertained in accordance with previously established methods [19]. Precisely 0.5 mL of the Gel solution was dispensed into a penicillin vial and subjected to constant agitation at 100 revolutions per minute. Subsequently, an equivalent volume of 0.5 mL of HA solution was introduced into the vial. This amalgamation was agitated vigorously until it solidified, thereby denoting the Gelation time of the HA-Gel cohort. Subsequently, to this consolidated mixture, 10.0 μg of NGF and 7 mg of Fe_3O_4 nanoparticles were meticulously incorporated and agitated until it regained a solidified state, thereby signifying the Gelation time of the HA-Gel@NGF + Fe_3O_4 ensemble.

Once Gelation was achieved, both hydrogel specimens underwent a freeze-drying process, which was sequentially followed by critical point drying and gold sputter coating for surface enhancement. For comprehensive analysis, at least three random microscopic fields were meticulously captured and documented.

Compression testing was carried out to evaluate the mechanical property by applying a strain rate of 1 mm/min using a universal testing system (CMT6103, USA). We determined the compressive modulus by taking the slope in the linear section of the stress-strain curve at 5%–10 % strain area. Three replicates were used for each group.

2.4. Hydrogel rheology test

In order to ascertain the definitive critical strain point of the hydrogel, an exhaustive strain amplitude scanning test was carried out at a consistent frequency of 1 Hz, encompassing a comprehensive strain spectrum spanning from 0.1 % to an extensive 1000 %. To evaluate the injectability characteristics of the HA-Gel@NGF + Fe_3O_4 hydrogel, we incorporated non-reactive trace dyes for enhanced visualization, enabling a clearer understanding of its flow properties. Subsequently, the hydrogel was delicately positioned within a syringe equipped with a precise 26-gauge needle, ensuring its seamless transfer. This arrangement facilitated the direct injection of the hydrogel onto a designated plate, further validating its suitability for injection-based applications.

2.5. Physical study of hydrogel paramagnetism and electrical conductivity

Spread the hydrogel evenly on the glass sheet. Slowly bring a magnet close to it and observe the morphology changes in the hydrogel and the distribution of Fe_3O_4 particles. Spread the hydrogel evenly on the glass sheet. Place the series circuit wires with LED lights at both ends of the hydrogel and observe if the LED lights illuminate.

2.6. In vitro HA response and in vivo degradation studies of hydrogel

The degradation behavior of HA-Gel@NGF + Fe_3O_4 was evaluated by wet weight loss. Briefly, 200 μL of hydrogel was immersed in 1 mL of PBS containing 100 U mL-1 hyaluronidase at 37 °C. The residual weight of the hydrogel was recorded on days 0, 8, 16, 24, and 32.

Using a calibrated 26-gauge needle, a precise volume of 1 mL of hydrogel was meticulously infused into the subcutaneous tissue located at the back of a healthy mouse. Following this injection, meticulous records were maintained to track the residual hydrogel at distinct intervals. During each assessment period, the mouse's skin was delicately excised in a manner that exposed the hydrogel without causing any unnecessary harm. This step allowed for a clear visualization of the hydrogel's interaction with the surrounding tissue. Furthermore, to capture this interaction in detail, both the hydrogel itself and the adjacent skin area were meticulously photographed.

The dosage of NGF was based on earlier studies that demonstrated that this concentration of NGF significantly promotes the repair of SCI

[20]. The NGF was used in a variety of applications, including the repair of SCI. *In vitro* release assessment method: lysozyme (lys, Sigma) was used with a molecular weight of 14.7 kD and an isoelectric point (pI) of 10.5. lys was used as an alternative to NGF due to its similar molecular weight and charge to NGF and its cheap and easy availability [21]. To enhance the lys assay process, fluorescein isothiocyanate (FITC) labeling was conducted on lys. Here's a detailed outline of how the FITC labeling on lys was accomplished: Firstly, FITC and lys were meticulously combined in distilled water, maintaining a precise weight ratio of 5:95. This mixture was then agitated at a temperature of 4 °C for an extended period of 8 h to ensure thorough mixing. Subsequently, the resulting solution underwent dialysis to purify it, followed by freeze-drying to produce FITC-labeled lys, ready for further use. In the next step, a blend comprising Gel, HA solution, and the FITC-labeled lys was carefully poured into a cylindrical vial, boasting a diameter of 16 mm. This vial was then immersed in a water bath, maintained at 37 °C, allowing the components to react and form a hydrogel. To assess the degradation properties of this hydrogel, PBS (either plain or supplemented with hyaluronidase) was gently introduced into the vials. These vials were then positioned in an oscillating incubator, set at a temperature of 37 °C and a rotational speed of 70 rpm. Over time, PBS samples were systematically collected at predetermined intervals, and fresh buffer was replenished to maintain the experimental conditions. The cumulative release of lys into the PBS was quantitatively determined by utilizing a multifunctional enzyme marker (Tecan Infinite M200, Switzerland). This instrument precisely measured the fluorescence intensity of FITC, with the excitation wavelength held constant at 495 nm, while the emission spectrum was scanned within the range of 510 nm–530 nm. This methodical approach provided a reliable and accurate assessment of the lys release dynamics within the hydrogel system.

2.7. Cytotoxicity test

The cytotoxicity of the hydrogel was meticulously evaluated through a comprehensive approach, encompassing both dead-viable staining and the CCK-8 (thiazolyl blue) viability assay. Here's a detailed account of the experimental methodology. Experimental Methods: Phenochromocytoma cells 12 (PC-12), serving as our cellular model, were strategically inoculated into hydrogel-embedded 24-well plates at distinct time points: 1 day, 3 days, and 5 days post-inoculation. To differentiate live from dead cells, we employed a sophisticated staining procedure utilizing the Calcium Xanthophyllin (Calcein-AM) AM/PI/Propidium Iodide (PI) Double Stain Kit sourced (Yeasen. Shanghai). This kit contains two vital fluorescent dyes: 2 μM troponin AM, which selectively stains viable cells green, and 2 μM thiazolyl blue, alongside an additional 4.5 μM of PI for staining non-viable cells red. Prior to staining, the medium was meticulously replaced with a PBS solution fortified with the aforementioned dyes. Subsequently, the plates were incubated for 30 min to ensure optimal staining efficacy. This visual differentiation enabled us to meticulously observe the cellular response under confocal laser scanning microscopy (CLSM), revealing a vivid contrast between the live (green) and dead (red) cells. Parallelly, to further substantiate our cytotoxicity assessment, PC-12 cells were separately incubated with electroactive hydrogels in 96-well plates for durations of 24 and 48 h. Following these incubations, 10 μL of CCK8 solution (Servicebio, G4103) was introduced to each well, and the incubation continued for an additional 2 h. The resulting absorbance at 450 nm, a direct indicator of cell viability, was precisely quantified using a Thermo enzyme labeling instrument. This comprehensive analysis, combining both qualitative and quantitative assessments, provided a robust evaluation of the hydrogels' cytotoxicity profile.

2.8. In vitro assessment of axonal growth

PC-12 cells were cultivated in Dulbecco's Modified Eagle's Medium (DMEM), which was enriched with 10 % heat-inactivated horse serum and 5 % fetal bovine serum (both sourced from Gibco), within a humidified incubator set at 37 °C and supplemented with 5 % CO2. These cells underwent passaging procedures every two days, utilizing a 1:2 dilution method with 0.25 % trypsin for dissociation. Subsequently, the cells were carefully seeded onto 14 mm diameter lids, pre-coated with poly-L-lysine at a density of 5 × 10^4 cells per well. These seeded cells were then inoculated onto culture plates, each containing distinct substrates: slides (serving as the control), hydrogel (HA-Gel), hydrogel fortified with NGF and Fe_3O_4 nanoparticles (HA-Gel@NGF + Fe_3O_4), and hydrogel supplemented with NGF, Fe_3O_4 nanoparticles, and an external magnetic field (HA-Gel@NGF + Fe_3O_4+MF). To establish the external magnetic field, a NdFeB magnet square was positioned parallel to the edge of the incubation plate, maintaining a distance of 10 cm. This setup generated a stable 300 MT magnetic field. The plates were then incubated at 37 °C, with a 5 % CO2 atmosphere. After a three-day incubation period, the neurite morphology was meticulously evaluated using confocal laser scanning microscopy (CLSM). Prior to imaging, the cells were stained with 4 % paraformaldehyde and 2 % FITC dissolved in DMSO for 10 min at room temperature. Following staining, the cells were rinsed thoroughly three times, adhering strictly to the prescribed washing protocol. Finally, the length of the neurites was precisely measured, extending from the cell body to the neurite's terminal end, utilizing the ImageJ software (National Institutes of Health, Bethesda, MD, USA).

2.9. In vitro cell development studies

Continue to propagate the previously acquired PC12 cells onto culture plates that are coated with a diverse array of substrates, including control, HA-Gel, HA-Gel@NGF + Fe_3O_4, and HA-Gel@NGF + Fe_3O_4+MF. At the seventh day mark, a comprehensive immunofluorescence analysis was conducted, utilizing neuron-specific markers such as class III βtubulin (TUJ1) and recombinant growth-associated protein 43 (GAP43) for staining. To ensure thorough examination, three distinct random fields were photographed using an advanced inverted microscope (Axio Vert. A1, manufactured by Leica, Germany), capturing the intricate details of the cellular response.

2.10. Surgical procedures and treatment of rats

SD rats were induced into a state of anesthesia utilizing 2 % isoflurane, enabling the creation of a precisely targeted 2 mm rectangular defect centered precisely on the T10 vertebrae. For the purposes of this study, five distinct subgroups were meticulously established: 1. Sham Group: This cohort underwent the surgical procedure involving the opening of the vertebral plate, but crucially, no SCI was inflicted. 2. Injury Group: Following the induction of SCI, this group was left untreated, providing a baseline for comparison. 3. HA-Gel@NGF Group: To further augment the healing process, HA-Gel hydrogel enriched with NGF was precisely placed within the injured area. 4. HA-Gel@NGF + Fe_3O_4 Group: HA-Gel hydrogel, enriched not only with NGF but also with Fe_3O_4 nanoparticles, was meticulously implanted in the injured site. 5. HA-Gel@NGF + Fe_3O_4+MF Group: The implantation of HA-Gel hydrogel enriched with both NGF and Fe_3O_4 nanoparticles, followed by the administration of magnetic mechanical force stimulation for a duration of 8 h daily. Specifically, an NdFeB magnet was strategically positioned over the surgical incision post-modeling, subsequently secured in place with dressings. This comprehensive treatment protocol aimed to maximize the regenerative potential. Ultimately, the incision site, encompassing both muscle and skin, was meticulously closed using sterile, needle-bearing sutures. Postoperatively, cefuroxime was administered via intraperitoneal injection to prevent infection, allowing the rats to awaken naturally at room temperature.

2.11. Spinal cord functional recovery assessment

Each experimental group was evaluated using the BBB score and electrophysiologic examination. To assess the recovery of lower extremity function, the BBB score scale was utilized weekly for 12 weeks postoperatively, enabling a detailed analysis of the motor function recovery process [22].

At the 12th week post-SCI, footprint experiments were conducted. The plantar surfaces of both hind feet of each rat were painted black using non-toxic ink, and the rats were then permitted to perform the footprint experiment on a pristine white paper track (measuring 21 × 59.4 cm^2). The measurements encompassed stride length, calculated as the distance between the centers of adjacent footprints on the same side, and sway distance, defined as the vertical separation between the centers of the right and left hindlimbs. Statistical comparisons were derived from the average values obtained from five steps for each case.

Twelve weeks after surgery, motor evoked potential (MEP) testing was performed. The rats were anesthetized with a mixture of isoflurane and 2 % oxygen, and they were positioned on a stereotaxic apparatus. The skin at the posterior aspect of the skull was meticulously disinfected with povidone-iodine, and a full-length incision was made to reveal the skull. Subsequently, the periosteum was delicately peeled away. A precisely drilled round hole with a diameter of 5 mm was created using a dental drill, positioned 3 mm posterior to the coronal suture line and 1 mm lateral to the sagittal suture line, directly in the center of the right cortex. Additionally, the skin on the left lateral thigh was incised, and the sciatic nerve was carefully exposed by separating the posterior femoral muscular space from the femur's posterior surface. The electrodes were positioned as follows: the positive electrode was situated in the cerebral cortex, the negative electrode was placed beneath the scalp, the recording electrode was inserted into the sciatic nerve, and the ground electrode was attached to the skin of the rat's tail. The stimulation parameters were meticulously set at a voltage intensity of 3 V, an amplitude of 1 ms, a frequency of 10 Hz, a gain of 20 times, and a filter of 300 Hz.

2.12. Spinal cord tissue dissection and HE and LFB staining

Spinal cord tissue dissection and Hematoxylin and Eosin (H&E) and Luxol fast blue (LFB) staining were performed 12 weeks after surgery. The procedure was performed as follows: rats were deeply anesthetized by intraperitoneal injection of 2 % sodium pentobarbital (at a dose of 50 mg/kg). After cardiac perfusion with 4 % paraformaldehyde was performed. Then the T9-T11 spinal cord was quickly dissected, fixed with 4 % (w/v) paraformaldehyde overnight, and 14-μm horizontal sections were cut on a cryostat (Leica CM 1900), and then stained for histological studies.

2.13. Immunofluorescence analysis

The T9-T11 segment was excised meticulously and submerged in a chilled 1× PBS solution containing 4 % PFA for a period of 24 h. After this initial fixation, the spinal cord tissue underwent a precise dissection process before being subjected to cryopreservation in 20 % and 30 % sucrose solutions, each for 24 h at 4 °C. Subsequently, the spinal cord was rapidly frozen in liquid nitrogen and stored at −80 °C for future use. To obtain precise horizontal sections, a cryostat (Leica CM 1900) was employed to cut 14 μm thick slices. These sections were then rigorously washed three times with 0.01 M PBS and incubated overnight at 4 °C with primary antibodies, chosen for their specificity to target antigens. The primary antibodies utilized in this study included mouse monoclonal antibodies directed against GAP43 (Proteintech, 16971-1-AP, diluted 1:100) and TUJ1 (Proteintech, 66375-1-lg, diluted 1:100), both markers of immature neurons. Additionally, anti-CHSY1 (Proteintech, 14420-1-AP, diluted 1:100) was used to label chondroitin sulfate proteoglycans (CSPGs), while anti-NF200 (Proteintech, 18934-1-AP, diluted 1:100) targeted neurofilament protein. SOD1 (Proteintech, 10269-1-AP, diluted 1:100) served as a marker for superoxide dismutase, and CD206 (Proteintech, 18704-1-AP, diluted 1:100) and CD68 (Proteintech, 28058-1-AP, diluted 1:100) were employed to identify M2-type macrophages. Following the primary antibody incubation, the spinal cord sections were washed three more times with PBS. The secondary antibody solution, consisting of Alexa Fluor 488 goat anti-rabbit antibody (Abcam, diluted 1:100) and Alexa Fluor 594 goat anti-mouse (Thermo, diluted 1:500), was then added to the sections and incubated for 1.5 h at 37 °C, with meticulous care taken to protect the samples from light exposure. Upon completion of the secondary antibody incubation, the sections were washed three more times with PBS and incubated with DAPI for 3 min in the dark to stain the nuclei. Excess DAPI was removed through PBS washes, and the slides were subsequently mounted with glycerol and coverslips. Finally, fluorescence microscopy (BX-51; Olympus) was utilized to capture images of randomly selected fields of view from each group.

2.14. Hydrogel toxic effects on tissues and organs in vivo

During the postoperative 12th week, while performing the dissection of the spinal cord tissue, the heart, liver, kidneys, lungs, and spleen were removed and fixed overnight in 4 % (w/v) paraformaldehyde, dehydrated with gradient ethanol, and embedded in paraffin. The tissue blocks were cut into 4 μm thick sections and stained with H&E for histological analysis.

3. Results and discussion

3.1. Preparation and characterization of HA-Gel@NGF + Fe_3O_4 hydrogel

HA-Gel@NGF + Fe_3O_4 hydrogel by chemical cross-linking method. Gel and HA can be reacted in the presence of EDC catalyst. HA-Gel hydrogel loaded with NGF and Fe_3O_4 nanoparticles was prepared by combining 1 mL of HA-Gel copolymer with 10.0 μg of NGF and 7 mg of Fe_3O_4 nanoparticles at 4 °C with gentle stirring (Fig. 2A). The infrared characteristic peak of Gel is at 1635cm-1 in the amide I band, 1535cm-1 in the amide II band and 1245cm-1 in the amide III. The infrared characteristic peak of HA is a stretching vibration peak of C=O at 1603cm-1 in the amide I band, C=O expansion vibration peak at 1405cm-1,1075cm-1 and bending vibration peak of CH and C-O-C at 1042 cm-1in the amide II band (Fig. 2B). The characteristic peak of Gel is obvious at 1535cm-1, while HA has no obvious vibration peak at 1535cm-1, and it is obvious in HA-Gel at 1535cm-1. This may be that a large number of amide bonds are formed after the reaction of HA-Gel, which makes the C=O characteristic peak of amide 1 band of HA shifts left and makes the wavelength increase (Fig. 2B). Therefore, it can be proved that the hydrogel synthesis of Gel and HA was successful.

The saturation magnetization of HA-Gel@NGF+7 mg Fe_3O_4 hydrogel is 62 emu/g; whereas with the decrease in feed ratio, the saturation magnetization of HA-Gel@NGF + Fe_3O_4 gradually decreases. The saturation magnetization of HA-Gel@NGF+5 mg Fe_3O_4 hydrogel is 33 emu/g; HA-Gel@NGF+3 mg Fe_3O_4 hydrogel is 20 emu/g; and the saturation magnetization of HA-Gel@NGF+0 mg Fe_3O_4 hydrogel is nearly 0 emu/g. This is due to the fact that other components of the hydrogel is not magnetic. The magnetic hysteresis loop analysis results a indicate that with the decrease in the feed ratio of Fe_3O_4, the material's response to the magnetic field weakens (Fig. 2C).

The lyophilized HA-Gel@NGF + Fe_3O_4 hydrogel had a microporous structure with an average pore size of 74.22 ± 11.01 μm (Fig. 2D), whereas the average pore size of the lyophilized HA-Gel hydrogel was 66.28 ± 8.21 μm (Fig. S1, Supporting Information). The Gelation time of the HA-Gel@NGF + Fe_3O_4 hydrogel was about 27.94 s, which was similar to that of the HA-Gel hydrogel of 26.9 s was similar to that of HA-Gel hydrogel (Fig. S1, Supporting Information).

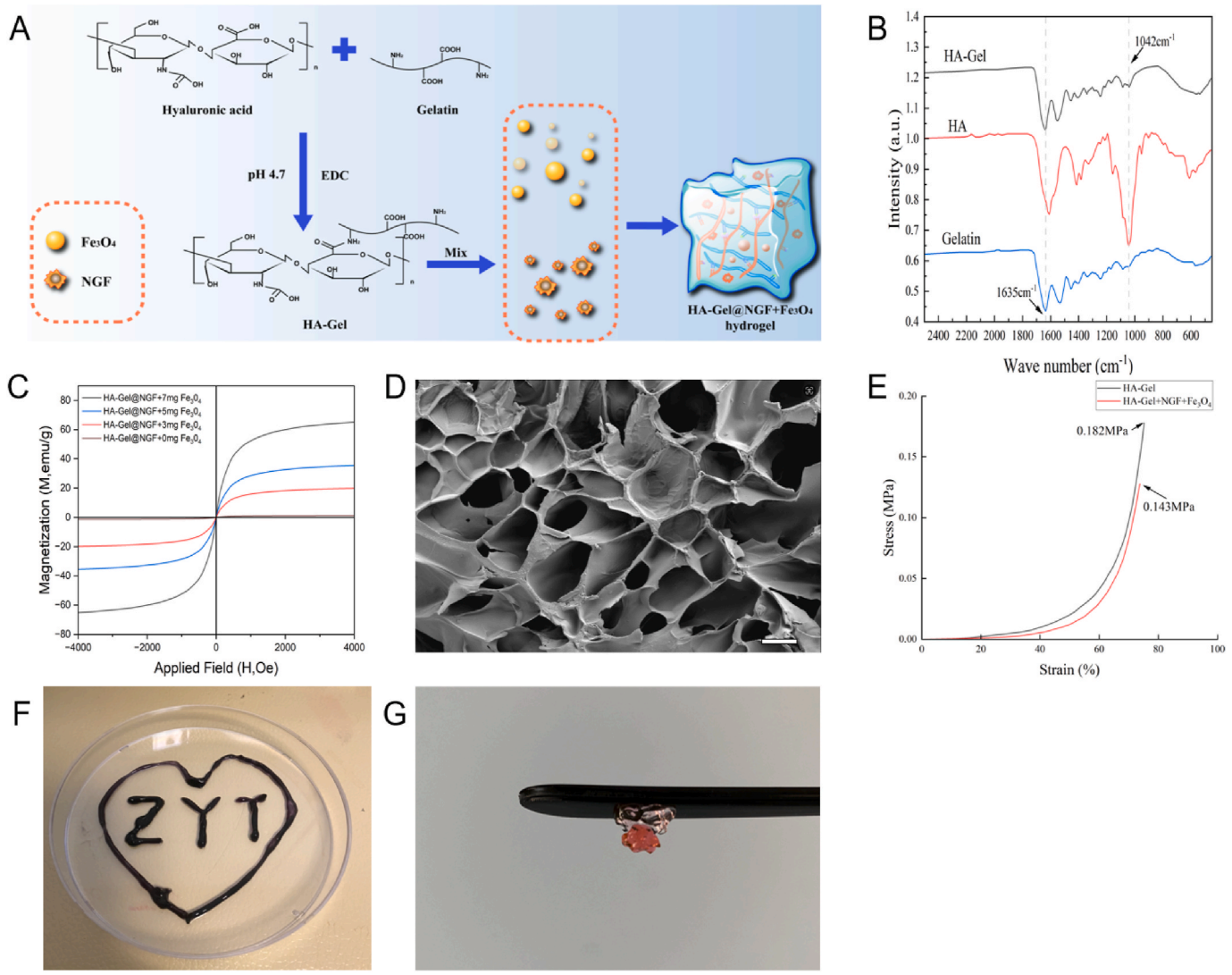

Fig. 2. Formation and characterization of HA-Gel@NGF + Fe_3O_4 hydrogel. (A) Schematic illustration of the synthesis of HA-Gel@NGF + Fe_3O_4 hydrogel. (B) FTIR spectra of Gel, HA, and HA-Gel. (C) The magnetic hysteresis loop of different Fe_3O_4 feed ratios. (D) SEM analysis of the freeze-dried hydrogel structure. Scale bar = 50 μm. (E) Stress-strain curves of the hydrogel under a consistent frequency of 1 Hz. (F) Image showing the injection of HA-Gel@NGF + Fe_3O_4 hydrogel from a 26-gauge needle, with no blockage. (G) Macroscopic image demonstrating the injectable and self-healing properties of the hydrogel.

Stress-strain curves of HA-Gel and HA-Gel@NGF + Fe_3O_4 (Fig. 2E). Creating hydrogels by utilizing electrostatic interactions between multivalent ions and natural polymers is a viable method [23]. Metal ions can form stable hydrogel structures through interaction with the carboxyl or hydroxyl groups of natural hydrogel [24]. Importantly, this crosslinking process can be completed at room temperature and physiological pH values. As shown in Fig. 2E, despite a slight decrease in the stress value of the hydrogel after the addition of NGF and Fe_3O_4, none of the samples ruptured when the compressive strain reached 75 %, demonstrating good compressive resistance. All samples exhibited smooth stress-strain curves. This indicates that Fe^{3+} ions may have crosslinked with the hydroxyl groups of HA, thereby reducing the loss of gel stress values. The mechanical properties of the hydrogel were characterized by uniaxial compression experiments. The compressive moduli of HA-Gel and HA-Gel@NGF + Fe_3O_4 were 29.80 ± 6.13 kPa and 28.02 ± 5.60 kPa, respectively (Fig. 1, Supporting Information). The compressive strength of HA-Gel@NGF + Fe_3O_4 was 42.30 ± 5.15 kPa. where the compressive strength of HA-Gel was quite large (46.58 ± 8.41 kPa) (Fig. S1, Supporting Information).

Macroscopic and rheological recovery tests were used to investigate the self-healing and injection properties of HA-Gel@NGF + Fe_3O_4. The hydrogel could be injected continuously without clogging using a needle (Fig. 2F). Two separated pink and black hydrogel were integrated into a new single and intact hydrogel. By placing the hydrogel vertically, the integrated hydrogel can also slide down intact (Fig. 2G). These injectable and self-healing properties give hydrogel the potential to perform grafting and in situ injections.

3.2. *Hydrogel has good paramagnetism, electrical conductivity and HA responsiveness in vitro*

After spreading the hydrogel uniformly onto a glass sheet and then slowly approaching a magnet to it, the hydrogel forms a magneto-fluid-like property in the hydrogel complex because of the internal Fe_3O_4 nanoparticles that respond to the magnetic field and the uniform dispersion of the whole system (Fig. 3A). Meanwhile, the HA-Gel@NGF + Fe_3O_4 hydrogel lights up LED when it is energized (Fig. S1, Supporting Information). Taken together, the hydrogel exhibit certain magnetic and conductive properties of their own.

The samples were divided into two distinct groups: one immersed in plain PBS and the other in PBS supplemented with hyaluronidase. We observed that the rate of degradation of the hydrogel significantly

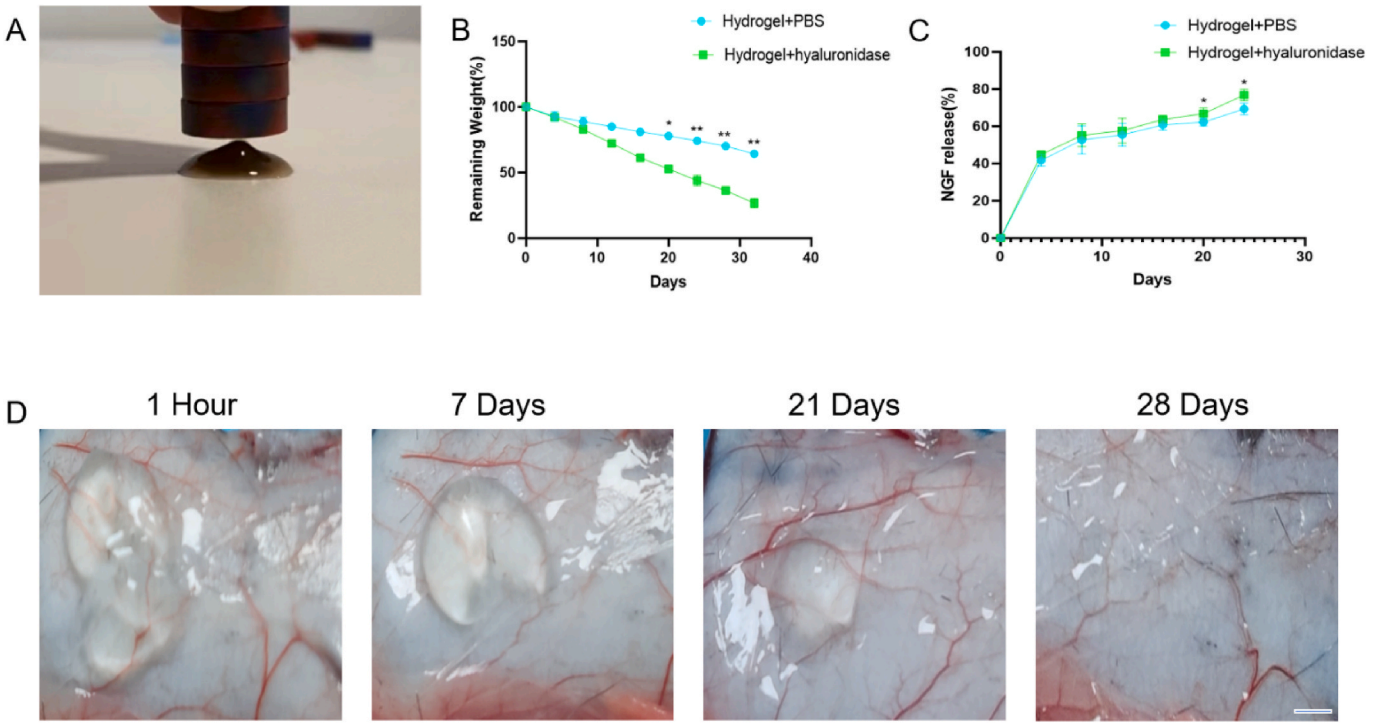

Fig. 3. Study on the Enzymatic/Magnetic Responsiveness of HA-Gel@NGF + Fe_3O_4 Hydrogel. (A) Physical photograph of the magnetic responsiveness of HA-Gel@NGF + Fe_3O_4 hydrogel. (B) Degradation curve of HA-Gel@NGF + Fe_3O_4 hydrogel. (C) NGF release curve of HA-Gel@NGF + Fe_3O_4 hydrogel. (D) Physical photograph of *in vivo* degradation of HA-Gel@NGF + Fe_3O_4 hydrogel. Scale bar = 0.5 cm.

accelerated in the presence of hyaluronidase, resulting in a substantial loss of over 73.4 ± 2.85 % of the hydrogel's mass within a period of 32 days (Fig. 3B). This finding underscores the hydrogel's moderate degradation rate, an attribute that renders it highly suitable for prolonged tissue repair applications. These results emphatically indicate the exceptional biodegradable properties of the hydrogel, alongside its responsiveness to hyaluronidase.

The prolonged deficiency of nutrients subsequent to SCI can hinder both the pace and ultimate extent of the repair process. Therefore, the capability of scaffolds to carry and deliver additional bioactive agents, ensuring a sustained nutrient supply for spinal cord repair, is of paramount importance. To this end, we delved into the release profile of NGF encapsulated within the hydrogel. Our investigation revealed that lysozyme, encapsulated alongside NGF, underwent a slight initial burst release of 41.80 ± 2.52 % within the first four days, likely due to the diffusion of lysozyme through the hydrogel matrix facilitated by water (Fig. 3C). To mimic the *in vivo* release of lysozyme as the hydrogel degrades, hyaluronidase was incorporated into the PBS solution, and the release pattern of lysozyme was continuously monitored. We discovered that approximately 76.78 ± 2.50 % of lysozyme was liberated from the hydrogel within 24 days post-addition of hyaluronidase, signifying the potential of NGF-laden hydrogel to steadily release NGF *in vivo* over extended periods, thereby fulfilling the NGF requirements of neuronal cells post-SCI.

To gain a deeper understanding of the degradation dynamics of hydrogel, we implanted this hydrogel subcutaneously in rats and cleaned the wound with saline as much as possible to maintain cleanliness. Our observations showed that the hydrogel gradually degraded over four weeks, and the degradation rate *in vivo* was slightly faster than what was observed *in vitro* (Fig. 3D).

3.3. *In vitro biocompatibility testing of hydrogel*

To comprehensively evaluate the *in vitro* cytotoxicity of the hydrogel, we employed a multifaceted approach involving both live and dead cell staining techniques alongside the CCK8 assay. By utilizing the ubiquitous and reputable commercial Live-Dead Staining Kit, we were able to simultaneously analyze the viability status of both viable and non-viable cells. This kit's dual-staining mechanism is predicated on the use of two distinct fluorescent dyes: LiveDye, a cell-permeable green fluorescent probe (Ex/Em = 488/530 nm) (AM), which selectively stains live cells, and NucleiDye, a non-permeable red fluorescent dye (Ex/Em = 535/617) (PI), designed to label dead cells [25]. Upon administering a cocktail of Calcein-AM and PI to co-cultured PC-12 cells, the fluorescence microscope revealed a vivid distinction between the living (green fluorescence) and deceased (red fluorescence) cells. Over the course of five days, PC-12 cells were co-incubated with the hydrogel, showcasing robust cellular proliferation and an absence of notable cell mortality, thereby attesting to the hydrogel's exceptional cellular compatibility (Fig. 4A). Complementing these findings, the CCK8 assay, renowned for its cost-effectiveness and efficiency in assessing cell survival and proliferation, was also deployed. This method has garnered widespread adoption in various domains, including the evaluation of bioactive factor activity, cytotoxicity assessments, and tumor radiosensitivity studies. Our CCK8 results revealed that after 24 h of co-culture, cell viability ranged from 96.05 ± 2.42 % to 97.32 ± 1.62 %, while at 48 h, this viability marginally declined but remained high, spanning 94.67 ± 1.65 % to 94.92 ± 3.07 % (Fig. 4B). In conclusion, the outcomes of this exhaustive experimental investigation underscore the hydrogel formulation's outstanding biocompatibility, underscoring its immense potential for diverse applications within the realm of tissue engineering.

3.4. *Hydrogel promotes cell proliferation and development*

Axons function as vital conduits, transmitting nerve impulses seamlessly from the neuronal cell body to adjacent neurons and effector cells, thereby facilitating the seamless transmission of motor and sensory functionalities. The intricate dynamics of PC12 cell line, as it undergoes metamorphosis into neuronal and glial cells, can be vividly observed through meticulous cultivation. Despite its origin from the chromaffin

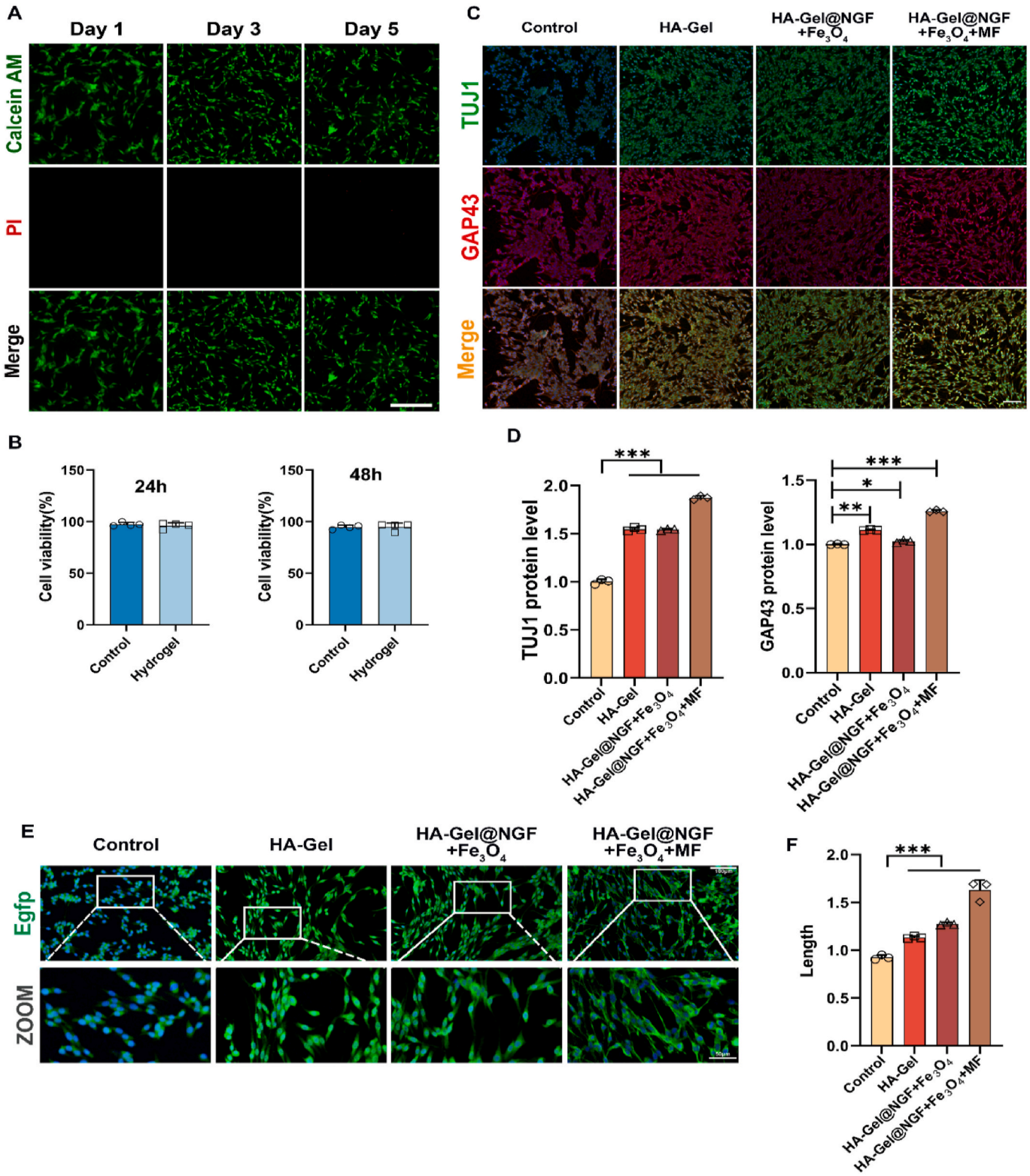

Fig. 4. Cytotoxicity study of HA-Gel@NGF + Fe_3O_4 hydrogel and PC12 cell axon growth study. (A) PC12 cells co-cultured with hydrogel and subjected to live-dead staining on days 1, 3, and 5. Scale bar = 100 μm. (B) Cell viability assay of PC12 cells co-cultured with hydrogel for 24 and 48 h. (C) Analysis of cell development by dual immunofluorescence labeling of TUJ1 (green) and GAP43 (red) after 7 days. Nuclei are stained with DAPI (blue). Scale bar = 50 μm. (D) Quantitative analysis of TUJ1 and GAP43 positive cell protein levels. Data are presented as mean ± standard deviation. ***P < 0.001. (E) Effect of hydrogel formulation on PC12 cell axon growth. Scale bar = 50 μm. (F) Quantitative analysis of axon length. Data are presented as mean ± SD (n = 3). ***P < 0.001.

tumor cell line within the adrenal medulla of mature rats, the PC12 cell line possesses a remarkable capacity for reversible neuronal deformation in response to NGF, devoid of epinephrine synthesis. Consequently, it has emerged as an exemplary cell line for delving into the intricacies of the central nervous system and has garnered widespread application. To authenticate the efficacy of our novel hydrogel in fostering axon growth, we embarked on a co-cultivation endeavor with PC-12 cells, subsequently analyzing the axon length of these cells. Our findings revealed a subtle trend towards axon protrusion among a select few PC-12 cells in the HA-Gel@NGF and HA-Gel@NGF + Fe_3O_4 cohorts. Conversely, the majority of PC-12 cells in the HA-Gel@NGF + Fe_3O_4+MF group exhibited robust neurite growth (Fig. 4E). A quantitative assessment of neurite lengths across various groups underscored the superiority of the HA-Gel@NGF + Fe_3O_4+MF group, with an average neurite length surpassing that of the control group, HA-Gel, and HA-Gel@NGF + Fe_3O_4 groups (Fig. 4F). These results underscore the limitations of relying solely on a single approach to augment neuronal axon growth. However, when this innovative hydrogel is synergistically combined with magnetic stimulation and NGF, a potent concerted effect comes into play, hinting at untapped potential. Nevertheless, the precise mechanisms underlying this synergy remain an enigma, warranting further exhaustive investigation.

TUJ1, a microtubule-associated protein, is hypothesized to play a pivotal role in the neuron-specific differentiation process [26]. Microtubule proteins constitute the fundamental structure of microtubules, which are essential components of the cytoskeleton that maintain cellular architecture, facilitate mitosis and meiosis, and regulate intracellular transportation, among other functions. Consequently, immunohistochemical staining techniques have demonstrated the presence of TUJ1 in the cytosol, dendrites, axons, and axon terminals of immature neurons. One of the key advantages of utilizing immunohistochemistry to detect TUJ1 lies in its exquisite capability to reveal intricate axonal and terminal details. Remarkably, it has proven invaluable in detecting alterations in cytoskeletal elements subsequent to damage. Intriguingly, despite the presence of a particular β-microtubule protein structure in glial cells, the TUJ1 antibody does not recognize it, resulting in substantial changes in neural differentiation within TUJ1-labeled neurons [27]. At the seventh day, the protein levels of TUJ1 in the HA-Gel@NGF + Fe_3O_4+MF group soared to 1.87, exceeding those observed in the control group (HA-Gel), as well as the HA-Gel-NGF@Fe_3O_4 groups (0.99, 1.54, and 1.53, respectively) (Fig. 4C and D). Numerous studies have underscored the paramount importance of GAP-43 protein in bolstering axon extension and preserving axon morphology [28]. Furthermore, GAP-43 protein exhibits a ubiquitous distribution within the synaptic region, while its presence in dendrites is minimal, implying its potential role in modulating neural signaling [29]. In the context of the HA-Gel@NGF + Fe_3O_4+MF group, the protein levels of GAP-43 at the seventh day attained a value of 1.27, surpassing those recorded in the control, HA-Gel, and HA-Gel-NGF@Fe_3O_4 groups (0.99, 1.11, and 1.02, respectively) (Fig. 4C and D). This compelling finding suggests that hydrogels fortified with NGF, in conjunction with magnetic stimulation, can orchestrate a synergistic effect, fostering the development of neuronal networks.

3.5. Recovery of motor function and signaling in SCI

In the intricate process of SCI remediation, the restoration of motor function emerges as the paramount evaluation criterion. To meticulously gauge the extent of motor function rejuvenation in SCI-afflicted rats post-treatment, we executed a comprehensive gait analysis and BBB scoring system [30]. Gait irregularities often stem from decreased muscular tone, cerebellar dysfunction, peripheral nerve impairment, or underlying musculoskeletal anomalies. At the 12-week mark post-surgery, we conducted footprint analysis for gait assessment. The sham control group displayed a steadfast and robust gait pattern, in stark contrast to the injured group, which exhibited shortened stride lengths and an increased step count, indicative of pronounced toe mobility deficiencies. Notably, all treatment cohorts demonstrated varying degrees of gait recovery, with the HA-Gel@NGF + Fe_3O_4+MF group exhibiting a gait pattern that most closely resembled the sham group, signifying optimal motor function recovery (Fig. 5A). Specifically, the HA-Gel@NGF, HA-Gel@NGF + Fe_3O_4, and HA-Gel@NGF + Fe_3O_4+MF groups recorded gait lengths of 6.0 ± 0.46 cm, 5.88 ± 0.50 cm, and 8.54 ± 0.74 cm, respectively. Notably, the HA-Gel@NGF + Fe_3O_4+MF group's gait length approached that of the sham group (11.54 ± 1.26 cm), highlighting its superior performance (Fig. 5B). Furthermore, in terms of swing distance, the HA-Gel@NGF + Fe_3O_4+MF group achieved 3.66 ± 0.12 cm, which was likewise proximate to the sham group's 2.08 ± 0.43 cm (Fig. 5C). This disparity in gait recovery might be attributed to the differential levels of conduction bundle and neuronal regeneration within the white and gray matter. Additionally, atrophic lower limb muscles contributing to inconsistent muscular tone also played a pivotal role in influencing the outcomes.

In order to meticulously track the restoration of motor function in rats with SCI, we administered BBB assessments at predetermined intervals. Subsequent to the surgical intervention, all groups, excluding the sham cohort, instantly exhibited hindlimb paralysis, with their BBB scores hovering near zero. The injured group failed to surpass a BBB score of 4 within the 12-week period, signifying the absence of compensatory recovery post-SCI.

Conversely, in the treatment groups, we observed a gradual upsurge in BBB scores over time. Commencing from the fourth postoperative week, rats belonging to the HA-Gel@NGF, HA-Gel@NGF + Fe_3O_4, and HA-Gel@NGF + Fe_3O_4+MF cohorts displayed notably elevated scores in comparison to their injured counterparts (Fig. 5D). At the 12-week mark post-surgery, the HA-Gel@NGF + Fe_3O_4+MF group boasted a BBB score of 13.8 ± 0.84, surpassing that of all other treatment groups. This underscores the potent capacity of the NGF-laden hydrogel, when combined with magnetic stimulation, to significantly augment the motor function recovery process subsequent to SCI.

To meticulously assess the reinstatement of nerve conduction function subsequent to SCI, we embarked on conducting MEP assessments. In the aftermath of SCI, where neural transmission routes are compromised, MEP parameters undergo corresponding alterations. Specifically, the amplitude of MEP diminishes, and the latency elongates in the injured cohort, exhibiting no discernible improvement trajectory over time.

Remarkably, after a period of 12 weeks, all therapeutic interventions elicited a pronounced enhancement in MEP amplitude, accompanied by a reduction in latency. Notably, the HA-Gel@NGF + Fe_3O_4+MF treatment arm displayed an amplitude of 2.37 ± 0.14 mV, surpassing that of both the HA-Gel@NGF and HA-Gel@NGF + Fe_3O_4 groups, which recorded values of 1.52 ± 0.08 and 1.61 ± 0.11 mV, respectively. Concurrently, the latency within the HA-Gel@NGF + Fe_3O_4+MF group shortened to 3.72 ± 0.18 ms, significantly shorter than that observed in the HA-Gel@NGF (6.82 ± 0.13 ms) and HA-Gel@NGF + Fe_3O_4 (4.2 ± 0.1 ms) groups (Fig. 5E). This comprehensive analysis underscores, from a different vantage point, the superior capacity of NGF-laden hydrogels, when synergistically employed with magnetic stimulation, to elicit the most optimal neural repair outcomes.

3.6. Repair of spinal cord tissue

Rats were executed 12 weeks after surgery and the spinal cord was completely stripped. We could see that all groups grew new tissue at the injury site, but since the injury model was only about 2 mm, it was difficult to distinguish the degree of repair of specific tissues and the composition of new tissues in different groups. Therefore, we further performed H&E staining. There was no tissue growth in the injury-only group, which was different from that observed by the naked eye, and this may be due to the obstruction of other surrounding tissues during the naked eye observation. The HA-Gel@NGF + Fe_3O_4+MF group had the

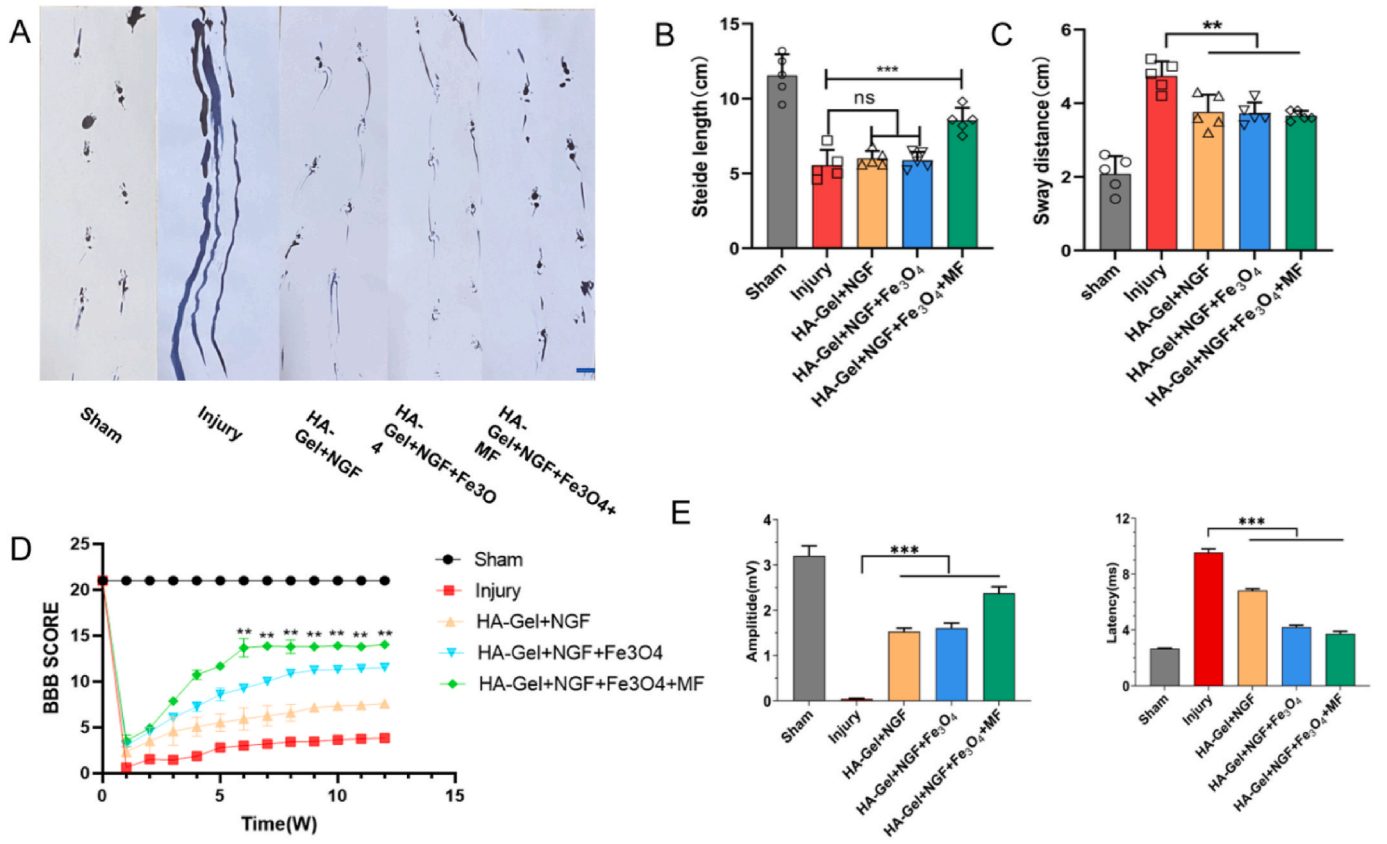

Fig. 5. Functional Recovery Following SCI. (A) Representative footprint patterns of different groups at 12 weeks post-SCI. Scale bar = 2.5 cm. (B) Semi-quantitative analysis of stride length in footprint tests. (C) Semi-quantitative analysis of swing distance in footprint tests. (D) BBB scores of rats at 12 weeks post-SCI. (E) MEP latency and amplitude. Data are presented as mean ± SD (n = 3). ***P < 0.001.

smallest lumen area and more new tissue compared to the other treatment groups (Fig. S2, Supporting Information). Thus, the results indicate that the HA-Gel@NGF + Fe_3O_4+MF preparation prepared by the present invention significantly promotes the growth and infiltration of nerve cells as well as the recovery of tissues. The LFB staining is specific to myelin; the blue areas show positive expression of myelin, while the pale areas represent demyelination. The incidence of demyelination was significant in the spinal cord injury group compared with the sham operation group. In contrast, HA-Gel@NGF + Fe_3O_4+MF showed better protection of myelin tissue compared to the SCI group (Fig. S2, Supporting Information).

3.7. Hydrogel in vivo improves the microenvironment of the damaged area and promotes neurogenesis

The hydrogel demonstrated an exceptional capacity to fill the void created by the transversely incised lesion. Twelve weeks subsequent to the injury, an intense manifestation of CSPGs was visibly detected through immunohistochemical staining utilizing the CS56 antibody at the site of the lesion (Fig. 6A). Within the lesion area, conspicuous positive staining of CSPGs was discernible, hinting at the presence of not just astrocytes, but also a substantial population of infiltrating cells that secrete CSPGs, congregating at the lesion periphery. While both HA-Gel@NGF and HA-Gel@NGF + Fe_3O_4 exhibited a tendency to mitigate the expression of CSPGs, quantitative evaluation revealed no statistically noteworthy divergence from the injury group (Fig. 6B). However, HA-Gel@NGF + Fe_3O_4+MF achieving a notable decrease in the deposition of CSPGs within the afflicted spinal cord. This reduction was corroborated by the sparse distribution of CSPGs deposits observed within the lesion site, underscoring the potential efficacy of this approach in modulating the inhibitory microenvironment.

Magnetic stimulation, as a non-invasive treatment method that can change the excitability of the brain or spinal cord, has received extensive attention from researchers and is mainly used to treat neurologic pain, stroke and other diseases [31–34]. It is evident that the immune factors within the diminutive glial cells present in the brains of rats that have been modeled with depression exhibit a notable surge. Subsequently to the implementation of magnetic stimulation therapy, there is a marked decrease in the activation of inflammatory glial cells, accompanied by a palpable alleviation of depressive and anxious symptoms [35]. Macrophages possess the capability to transform into various phenotypic manifestations. Specifically, the M1 phenotype contributes to the secretion of proinflammatory molecules, thereby intensifying the progression of secondary injury. Conversely, the M2 phenotype is instrumental in fostering axon and nerve regeneration. To discern the presence of M2 macrophages within the afflicted region, we employed spinal cord immunofluorescence staining (Fig. 6C). Intriguingly, although the abundance of CD68-positive cells was observed to be elevated in both the HA-Gel@NGF (4.78 ± 0.58) and HA-Gel@NGF + Fe_3O_4 groups (4.80 ± 0.37), as compared to the injury group (3.80 ± 0.50), it was solely within the HA-Gel@NGF + Fe_3O_4+MF group (4.40 ± 0.40) that the CD206 level demonstrated a statistically significant elevation over that of the injury group (2.84 ± 0.29). This observation implies that in the HA-Gel@NGF and HA-Gel@NGF + Fe_3O_4 groups, microglia/macrophages primarily exhibit CD68 positivity, whereas it is exclusively in the HA-Gel@NGF + Fe_3O_4+MF group that CD206-positive M2 macrophages are evident (Fig. 6D). After a period of two weeks during which low-frequency magnetic stimulation therapy was administered, the levels of MDA and SOD within the oxidative stress pathway of the hippocampus in rats modeled with vascular dementia underwent substantial improvement, leading to a notable enhancement in the cognitive abilities of these rats [36–38]. These findings align with

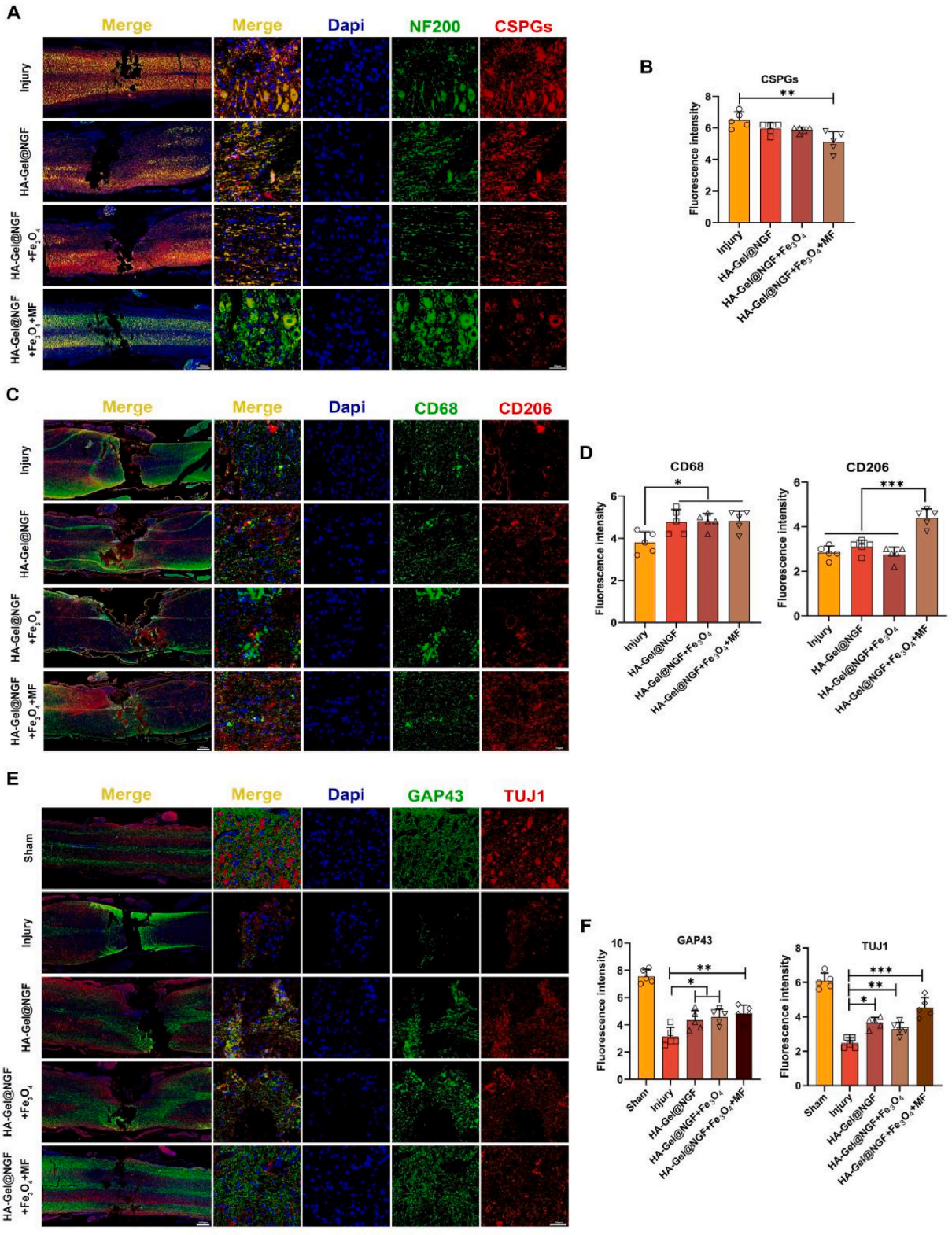

Fig. 6. The effect of HA-Gel@NGF + Fe_3O_4 hydrogel on the SCI microenvironment and axonal growth *in vivo*. (A) After 12 weeks of treatment, the CSPGs and neurogenesis in the injured environment were analyzed using double immunofluorescence labeling with CHSY1 (red) and NF200 (green). Nuclei were stained with DAPI (blue). Scale bar, 50 μm. (B) Quantitative analysis data of CHSY1 and NF200 fluorescence intensity are presented as mean ± SD (n = 5). *P < 0.05, **P < 0.001, ***P < 0.001. (C) After 12 weeks of treatment, the M2 macrophage condition in the injured environment was analyzed using double immunofluorescence labeling with CD68 (green) and CD206 (red). Nuclei were stained with DAPI (blue). Scale bar, 50 μm. (D) Quantitative analysis data of CD68 and CD206 fluorescence intensity are presented as mean ± SD (n = 5). *P < 0.05, ****P < 0.0001. (E) After 12 weeks of treatment, the neurogenesis in the injured environment was analyzed using double immunofluorescence labeling with GAP43 (green) and TUJ1 (red). Nuclei were stained with DAPI (blue). Scale bar, 50 μm. (F) Quantitative analysis data of GAP43 and TUJ1 fluorescence intensity are presented as mean ± SD (n = 5). *P < 0.05, **P < 0.001, ****P < 0.0001.

the outcomes of our research endeavors. The hydrogel, renowned for its exceptional biocompatibility, safeguards the compromised site from undue immune assault, whereas the application of an external magnetic field attenuates the expression of SOD-1. In essence, the synergistic action of the drug-laden hydrogel in conjunction with external magnetic stimulation optimizes the immune microenvironment at the site of injury, thereby fostering an environment conducive to axon sprouting and neural development (Fig. S3, Supporting Information).

In the present investigation, *in vitro* experimental endeavors have unequivocally affirmed the potent capacity of the hydrogel-magnetic stimulation pairing to foster neuronal expansion and maturation. To fortify this observation with *in vivo* evidence, we conducted a comprehensive double fluorescent staining analysis of spinal cord tissue, utilizing GAP43 and TUJ1 as markers. Notably, the injured group exhibited a conspicuous absence of tissue rejuvenation, whereas rats administered with HA-Gel@NGF and HA-Gel@NGF + Fe_3O_4 demonstrated varying levels of tissue restoration. Intriguingly, we discerned that GAP43 and TUJ1 exhibited differential expressions and a remarkable degree of colocalization within the newly formed tissues, hinting at the occurrence of endogenous neurogenesis (Fig. 6E). This process entails the migration of neuronal precursors from unharmed regions towards the damaged sites, subsequently transforming into functional neurons. Delving deeper, our semi-quantitative assessment unveiled that the HA-Gel@NGF + Fe_3O_4+MF cohort displayed significantly elevated levels of TUJ1 (4.84 ± 0.54) and GAP43 (4.54 ± 0.52) compared to their counterparts in the injured group (3.14 ± 0.61) and (2.48 ± 0.27) respectively (Fig. 6F). This notable augmentation underscores the enhanced efficacy of a multifaceted therapeutic approach rooted in drug-laden hydrogels, thereby emphasizing its superiority in fostering spinal cord repair.

3.8. Treatment of hydrogel had no obvious effect on significant organs in rats

To further understand the biocompatibility of hydrogels *in vivo*, we performed H&E staining on the skin and vital organs of rats that had received hydrogel treatment. The results showed that hydrogel treatment did not cause inflammatory reactions in the organs, indicating that the hydrogel has good biocompatibility *in vivo* and can be used for treatment within the body (Fig. 7).

4. Conclusion

In conclusion, this research groundbreakingly presents a novel hydrogel system, loaded with therapeutic agents, which is capable of responding to both hyaluronidase, a naturally occurring enzyme post-

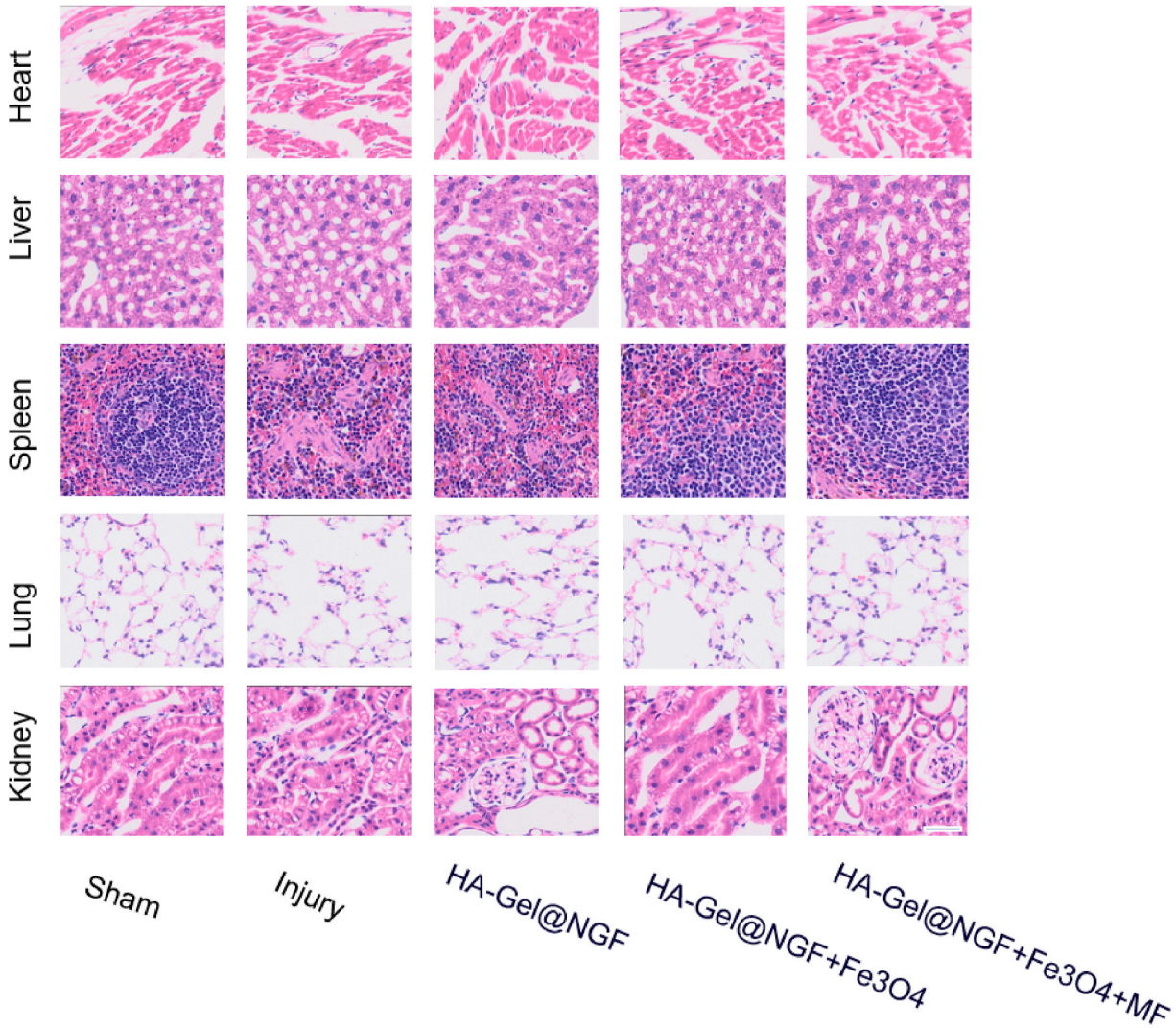

Fig. 7. Hydrogel toxic effects on tissues and organs *in vivo*. At the twelfth week post-operation, perform H&E staining on the vital organs of rats treated with HA-Gel@NGF + Fe_3O_4 hydrogel to observe for any significant inflammatory response. Scale bar = 100 μm.

SCI, and external magnetic stimuli. This advanced hydrogel deftly degrades and subsequently releases NGF in the presence of hyaluronidase, while its embedded nanoparticles adeptly respond to externally applied magnetic fields.

Not only does this hydrogel exhibit commendable mechanical stability and rheological characteristics, but it also boasts remarkable biocompatibility, potently mitigating inflammation, and fostering neurogenic recovery. The empirical findings underscore the hydrogel's efficacy in ameliorating motor dysfunction subsequent to SCI in rat models, thereby offering a promising therapeutic avenue for the treatment of this debilitating condition.

CRediT authorship contribution statement

Zhiyi Fan: Writing – original draft, Validation. **Guofu Zhang:** Validation. **Wanda Zhan:** Formal analysis. **Juehan Wang:** Formal analysis. **Chaoyong Wang:** Visualization. **QianYing Yue:** Writing – review & editing. **Zhangheng Huang:** Writing – review & editing, Visualization. **Yongxiang Wang:** Supervision, Project administration, Conceptualization.

Ethic statement

This study was approved by the Animal Experimental Ethics Committee of the Yangzhou University (yzu-lcyxy-n472). Animal feeding and welfare tests were performed according to the standards of the Laboratory of Yangzhou.

Funding

This work was supported by the National Key Research and Development Program of China (2023YFB3810200, 2023YFB3810204), the National Natural Science Foundation of China (82272502, 82072423), China Medical Education Association 2022 major scientific problems and key topics of medical technology problems (2022KTM022) and Yangzhou key research and development plan (social development) project (YZ2022070).

Declaration of competing interest

The authors declare that they have no known competing financial interests or personal relationships that could have appeared to influence the work reported in this paper.

Acknowledgment

Not applicable.

Appendix A. Supplementary data

Supplementary data to this article can be found online at https://doi.org/10.1016/j.mtbio.2024.101378.

Data availability

Data will be made available on request.

References

[1] N.A. Silva, R.A. Sousa, J.S. Fraga, M. Fontes, H. Leite-Almeida, R. Cerqueira, A. Almeida, N. Sousa, R.L. Reis, A.J. Salgado, Benefits of spine stabilization with biodegradable scaffolds in spinal cord injured rats, Tissue Eng. C Methods 19 (2) (2013) 101–108, https://doi.org/10.1089/ten.TEC.2012.0264.

[2] Y. Zhang, Z. Guan, B. Reader, T. Shawler, S. Mandrekar-Colucci, K. Huang, Z. Weil, A. Bratasz, J. Wells, N.D. Powell, J.F. Sheridan, C.C. Whitacre, A.G. Rabchevsky, M. S. Nash, P.G. Popovich, Autonomic dysreflexia causes chronic immune suppression after spinal cord injury, J. Neurosci. 33 (32) (2013) 12970–12981, https://doi.org/10.1523/jneurosci.1974-13.2013.

[3] C. Meisel, J.M. Schwab, K. Prass, A. Meisel, U. Dirnagl, Central nervous system injury-induced immune deficiency syndrome, Nat. Rev. Neurosci. 6 (10) (2005) 775–786, https://doi.org/10.1038/nrn1765.

[4] X. Li, Z. Xiao, J. Han, L. Chen, H. Xiao, F. Ma, X. Hou, X. Li, J. Sun, W. Ding, Y. Zhao, B. Chen, J. Dai, Promotion of neuronal differentiation of neural progenitor cells by using EGFR antibody functionalized collagen scaffolds for spinal cord injury repair, Biomaterials 34 (21) (2013) 5107–5116, https://doi.org/10.1016/j.biomaterials.2013.03.062.

[5] Y.F. Wang, J.N. Zu, J. Li, C. Chen, C.Y. Xi, J.L. Yan, Curcumin promotes the spinal cord repair via inhibition of glial scar formation and inflammation, Neurosci. Lett. 560 (2014) 51–56, https://doi.org/10.1016/j.neulet.2013.11.050.

[6] WHO, Spinal Cord Injury: as Many as 500 000 People Suffer Each Year, 2013.

[7] H. Li, T.R. Ham, N. Neill, M. Farrag, A.E. Mohrman, A.M. Koenig, N.D. Leipzig, A hydrogel bridge incorporating immobilized growth factors and neural stem/progenitor cells to treat spinal cord injury, Adv. Healthcare Mater. 5 (7) (2016) 802–812, https://doi.org/10.1002/adhm.201500810.

[8] S. Mura, J. Nicolas, P. Couvreur, Stimuli-responsive nanocarriers for drug delivery, Nat. Mater. 12 (11) (2013) 991–1003, https://doi.org/10.1038/nmat3776.

[9] R. Stern, A.A. Asari, K.N. Sugahara, Hyaluronan fragments: an information-rich system, Eur. J. Cell Biol. 85 (8) (2006) 699–715, https://doi.org/10.1016/j.ejcb.2006.05.009.

[10] Z.-Y. Yao, J. Qin, J.-S. Gong, Y.-H. Ye, J.-Y. Qian, H. Li, Z.-H. Xu, J.-S. Shi, Versatile strategies for bioproduction of hyaluronic acid driven by synthetic biology, Carbohydr. Polym. 264 (2021) 118015, https://doi.org/10.1016/j.carbpol.2021.118015.

[11] E. Chaik, E.S. Duthie, A mucolytic enzyme in testis extracts, Nature 144 (3658) (1939) 977–978, https://doi.org/10.1038/144977b0.

[12] R.O. Miura, S. Yamagata, Y. Miura, T. Harada, T. Yamagata, Analysis of glycosaminoglycan-degrading enzymes by substrate gel electrophoresis (zymography), Anal. Biochem. 225 (2) (1995) 333–340, https://doi.org/10.1006/abio.1995.1163.

[13] Y. Tachi, T. Okuda, N. Kawahara, N. Kato, Y. Ishigaki, T. Matsumoto, Expression of hyaluronidase-4 in a rat spinal cord hemisection model, Asian. Spine. J. 9 (1) (2015) 7–13, https://doi.org/10.4184/asj.2015.9.1.7.

[14] V. Neirinckx, D. Cantinieaux, C. Coste, B. Rogister, R. Franzen, S. Wislet-Gendebien, Concise review: spinal cord injuries: how could adult mesenchymal and neural crest stem cells take up the challenge? Stem Cell. 32 (4) (2014) 829–843, https://doi.org/10.1002/stem.1579.

[15] Y. Fujimoto, M. Abematsu, A. Falk, K. Tsujimura, T. Sanosaka, B. Juliandi, K. Semi, M. Namihira, S. Komiya, A. Smith, K. Nakashima, Treatment of a mouse model of spinal cord injury by transplantation of human induced pluripotent stem cell-derived long-term self-renewing neuroepithelial-like stem cells, Stem Cell. 30 (6) (2012) 1163–1173, https://doi.org/10.1002/stem.1083.

[16] M. Nakamura, Y. Toyama, H. Okano, Transplantation of neural stem cells for spinal cord injury, Rinsho Shinkeigaku 45 (11) (2005) 874–876.

[17] E.H. Javazon, K.J. Beggs, A.W. Flake, Mesenchymal stem cells: paradoxes of passaging, Exp. Hematol. 32 (5) (2004) 414–425, https://doi.org/10.1016/j.exphem.2004.02.004.

[18] M. Ma, Y. Zhang, W. Yu, H.-y. Shen, H.-q. Zhang, N. Gu, Preparation and characterization of magnetite nanoparticles coated by amino silane, Colloids Surf. A Physicochem. Eng. Asp. 212 (2) (2003) 219–226, https://doi.org/10.1016/S0927-7757(02)00305-9.

[19] J. Chen, H. Zhu, Y. Zhu, C. Zhao, S. Wang, Y. Zheng, Z. Xie, Y. Jin, H. Song, L. Yang, J. Zhang, J. Dai, Z. Hu, H. Wang, Injectable self-healing hydrogel with siRNA delivery property for sustained STING silencing and enhanced therapy of intervertebral disc degeneration, Bioact. Mater. 9 (2022) 29–43, https://doi.org/10.1016/j.bioactmat.2021.08.003.

[20] Y.Z. Zhao, X. Jiang, J. Xiao, Q. Lin, W.Z. Yu, F.R. Tian, K.L. Mao, W. Yang, H. L. Wong, C.T. Lu, Using NGF heparin-poloxamer thermosensitive hydrogels to enhance the nerve regeneration for spinal cord injury, Acta. Biomater. 29 (2016) 71–80, https://doi.org/10.1016/j.actbio.2015.10.014.

[21] B. Song, J. Song, S. Zhang, M.A. Anderson, Y. Ao, C.Y. Yang, T.J. Deming, M. V. Sofroniew, Sustained local delivery of bioactive nerve growth factor in the central nervous system via tunable diblock copolypeptide hydrogel depots, Biomaterials 33 (35) (2012) 9105–9116, https://doi.org/10.1016/j.biomaterials.2012.08.060.

[22] D.M. Basso, M.S. Beattie, J.C. Bresnahan, A sensitive and reliable locomotor rating scale for open field testing in rats, J. Neurotrauma 12 (1) (1995) 1–21, https://doi.org/10.1089/neu.1995.12.1.

[23] X. Liang, C. Huang, H. Liu, H. Chen, J. Shou, H. Cheng, G. Liu, Natural hydrogel dressings in wound care: design, advances, and perspectives, Chin. Chem. Lett. 35 (10) (2024) 109442, https://doi.org/10.1016/j.cclet.2023.109442.

[24] X. Liang, L. Ding, J. Ma, J. Li, L. Cao, H. Liu, M. Teng, Z. Li, Y. Peng, H. Chen, Y. Zheng, H. Cheng, G. Liu, Enhanced mechanical strength and sustained drug release in carrier-free silver-coordinated anthraquinone natural antibacterial anti-inflammatory hydrogel for infectious wound healing, Adv. Healthcare Mater. 13 (23) (2024) e2400841, https://doi.org/10.1002/adhm.202400841.

[25] Z. Fan, L. Ren, W. Zhang, D. Li, G. Zhao, J. Yu, AIE luminogen-functionalised mesoporous silica nanoparticles as nanotheranostic agents for imaging guided synergetic chemo-/photothermal therapy, Inorg. Chem. Front. 4 (5) (2017) 833–839, https://doi.org/10.1039/C7QI00046D.

[26] M.K. Lee, J.B. Tuttle, L.I. Rebhun, D.W. Cleveland, A. Frankfurter, The expression and posttranslational modification of a neuron-specific beta-tubulin isotype during chick embryogenesis, Cell Motil Cytoskeleton 17 (2) (1990) 118–132, https://doi.org/10.1002/cm.970170207.

[27] E.E. Geisert Jr., A. Frankfurter, The neuronal response to injury as visualized by immunostaining of class III beta-tubulin in the rat, Neurosci. Lett. 102 (2–3) (1989) 137–141, https://doi.org/10.1016/0304-3940(89)90068-2.
[28] E.E. Baetge, J.P. Hammangt, Neurite outgrowth in PC12 cells deficient in GAP-43, Neuron 6 (1) (1991) 21–30, https://doi.org/10.1016/0896-6273(91)90118-J.
[29] L.I. Benowitz, A. Routtenberg, GAP-43: an intrinsic determinant of neuronal development and plasticity, Trends Neurosci. 20 (2) (1997) 84–91, https://doi.org/10.1016/S0166-2236(96)10072-2.
[30] S. Girirajan, N. Patel, R.E. Slager, M.E. Tokarz, M. Bucan, J.L. Wiley, S.H. Elsea, How much is too much? Phenotypic consequences of Rai1 overexpression in mice, Eur. J. Hum. Genet. 16 (8) (2008) 941–954, https://doi.org/10.1038/ejhg.2008.21.
[31] H.R. Siebner, K. Funke, A.S. Aberra, A. Antal, S. Bestmann, R. Chen, J. Classen, M. Davare, V. Di Lazzaro, P.T. Fox, M. Hallett, A.N. Karabanov, J. Kesselheim, M. M. Beck, G. Koch, D. Liebetanz, S. Meunier, C. Miniussi, W. Paulus, A.V. Peterchev, T. Popa, M.C. Ridding, A. Thielscher, U. Ziemann, J.C. Rothwell, Y. Ugawa, Transcranial magnetic stimulation of the brain: what is stimulated? - a consensus and critical position paper, Clin. Neurophysiol. 140 (2022) 59–97, https://doi.org/10.1016/j.clinph.2022.04.022.
[32] A. Robac, P. Neveu, A. Hugede, E. Garrido, L. Nicol, Q. Delarue, N. Guérout, Repetitive trans spinal magnetic stimulation improves functional recovery and tissue repair in contusive and penetrating spinal cord injury models in rats, Biomedicines 9 (12) (2021) 1827, https://doi.org/10.3390/biomedicines9121827.
[33] C. Chalfouh, C. Guillou, J. Hardouin, Q. Delarue, X. Li, C. Duclos, D. Schapman, J. P. Marie, P. Cosette, N. Guérout, The regenerative effect of trans-spinal magnetic stimulation after spinal cord injury: mechanisms and pathways underlying the effect, Neurotherapeutics 17 (4) (2020) 2069–2088, https://doi.org/10.1007/s13311-020-00915-5.
[34] J. Luo, Y. Feng, Z. Hong, M. Yin, H. Zheng, L. Zhang, X. Hu, High-frequency repetitive transcranial magnetic stimulation promotes neural stem cell proliferation after ischemic stroke, Neural Regen. Res. 19 (8) (2024) 1772–1780, https://doi.org/10.4103/1673-5374.389303.
[35] S.F. Feng, T.Y. Shi, Y. Fan, W.N. Wang, Y.C. Chen, Q.R. Tan, Long-lasting effects of chronic rTMS to treat chronic rodent model of depression, Behav. Brain Res. 232 (1) (2012) 245–251, https://doi.org/10.1016/j.bbr.2012.04.019.
[36] X. Liao, G. Li, A. Wang, T. Liu, S. Feng, Z. Guo, Q. Tang, Y. Jin, G. Xing, M. A. McClure, H. Chen, B. He, H. Liu, Q. Mu, Repetitive transcranial magnetic stimulation as an alternative therapy for cognitive impairment in Alzheimer's disease: a meta-analysis, J. Alzheimers Dis. 48 (2) (2015) 463–472, https://doi.org/10.3233/jad-150346.
[37] F. Wang, G.M. Chang, Q. Yu, X. Geng, The neuroprotection of repetitive transcranial magnetic stimulation pre-treatment in vascular dementia rats, J. Mol. Neurosci. 56 (1) (2015) 198–204, https://doi.org/10.1007/s12031-014-0480-7.
[38] N. Zhang, M. Xing, Y. Wang, H. Tao, Y. Cheng, Repetitive transcranial magnetic stimulation enhances spatial learning and synaptic plasticity via the VEGF and BDNF-NMDAR pathways in a rat model of vascular dementia, Neuroscience 311 (2015) 284–291, https://doi.org/10.1016/j.neuroscience.2015.10.038.